Nodal trajectories of spin observables and kaon photoproduction dynamics

Bijan Saghai
Service de Physique Nucléaire, CEA/DSM/DAPNIA, Centre d'Études de Saclay, F-91191 Gif-sur-Yvette, France

Frank Tabakin
Department of Physics and Astronomy, University of Pittsburgh, Pittsburgh, Pennsylvania 15260

(Received 25 August 1995)

Spin observables for the reaction $\gamma p \to K^+\Lambda$ are examined using three recent dynamical models and are compared to the general features of such observables deduced earlier by Fasano, Tabakin, and Saghai. These general features, such as the energy dependence of spin observables and the location of nodes in their angle dependence, are realized. Several instructive surprises, which occur in this comparison to the conjectures of Fasano *et al.*, are then discussed. The sensitivity of spin observables to isobar and *t*-channel dynamics is analyzed and suggestions for selecting experiments which provide important dynamical information are presented.

PACS number(s): 24.70.+s, 25.20.Lj, 13.60.Le, 13.88.+e

I. INTRODUCTION

The measurement of almost complete sets of spin observables has become technically feasible because newly developed polarized electron or photon beams and polarized targets offer high enough luminosity to permit measurement of the relevant observables. The reaction $\gamma + p \to K^+ + \Lambda$ is particularly advantageous, since the angular asymmetry in the parity nonconserving weak decay $\Lambda \to p + \pi^-$ provides a direct measurement of the Λ's polarization. If the Λ's spin state is measured along with the polarization of the beam (γ) or target (p), then spin transfer and spin rotation observables can be measured. Such spin-rich experiments are underway at ELSA [1] and planned at CEBAF [2] and GRAAL [3].

In an earlier publication [4] (FTS), the general structure of the full set of 16 observables for K^+ photoproduction was examined. In that discussion, helicity amplitudes proved to be particularly useful for deducing general rules concerning the angular structure of the 15 spin observables. The 16 observables (the cross section plus 15 spin observables) were found to fall into four ''Legendre classes,'' with four members in each class. The observables in each class have similar ''nodal structure'' possibilities, e.g., their values at 0° and 180° and their possible intervening nodes are of related nature. (That classification procedure, along with the advantages of transversity amplitudes, has led to a reformulation of the general problem of determining which experiments constitute a complete set of measurements. A generalization to many reactions, including electroproduction and photoproduction of vector mesons, will be published separately [5].)

In addition, FTS used various truncations, both in a helicity basis and in a multipole representation, to deduce rules concerning the nodal structure and energy evolution of all 15 spin observables. In this paper, those FTS rules are confronted with specific dynamical models. The considered models [6–8] are all based on an isobaric approach using diagrammatic techniques. These models include extended Born terms and a very limited number of resonances in *s* and *u* channels supplemented by contributions from the *t* channel; namely, by $K^*(892)(1^-)$ and $K1(1270)(1^+)$ as well as K^+ meson exchanges.

We now comment briefly on each model and give the relevant baryonic resonances. To aid in comparing the reaction mechanisms of each dynamical model we present their exchanged particles, isobars, and associated coupling constants in Table I. First, the model of Adelseck and Saghai (AS) [6] is used to calculate the spin observables. Their model, which represents a good fit ($\chi^2/N_{\rm DF} \simeq 1.4$), to the existing data up to $E_\gamma^{\rm lab} \leqslant 1.5$ GeV, uses the $N^*(1440)1(1/2^+)$ and $\Lambda^*(1670)0(1/2^-)$ baryon resonances.[1] In addition, SU(3) constraints, based on their success in strong interaction dynamics, are used to limit an otherwise oversupply of possible fits to the data. Then, we also study the work of Williams, Ji, and Cotanch (WJC) [7], who examined electromagnetic production processes with photons (real and virtual) energies up to 2.1 GeV. That group included the $N^*(1650)0(1/2^-)$, $N^*(1710)1(1/2^+)$, and $\Lambda^*(1405)0(1/2^-)$ baryon exchanges, plus a significant incorporation of crossing symmetry requirements.

The third dynamical model considered here is a new model from the Saclay-Lyon Group called SALY [8], which also gives good agreement with photoproduction data up to 2.1 GeV and satisfies broken SU(3) symmetry requirements. The SALY model includes all of the above AS baryon resonances plus the $N^*(1700)2(3/2^-)$, $N^*(1720)1(3/2^+)$, and $\Lambda^*(1600)1(1/2^+)$ baryon resonances. We emphasize that the first two models (AS and WJC) include only spin-1/2 baryonic resonances, while the third one (SALY) also includes spin-3/2 nucleonic resonances. Spin-5/2 resonances are not included in any of these models.

Among these three models, the WJC model has the weakest kaon exchange (*t*-channel) contributions, while AS has the strongest. The WJC model produces weak *t*-channel ex-

[1]The quantum numbers of the baryons are indicated as $\not{\ell}_{K\Lambda}(J^\pi)$.

TABLE I. Exchanged particles, isobars, and coupling constants of the three dynamical models: AS [6], WJC [7], and SALY [8].

Particle	$\ell(J\pi)$	Coupling	AS	WJC	SALY
Λ		$g_{K\Lambda N}/\sqrt{4\pi}$	-4.17 ± 0.75	-2.38	-3.16 ± 0.03
Σ^0		$g_{K\Sigma N}/\sqrt{4\pi}$	$+1.18\pm0.66$	$+0.27$	$+0.79\pm0.03$
$K^*(892)$	(1^-)	$G_V/4\pi$	-0.43 ± 0.07	-0.16	-0.19 ± 0.01
		$G_T/4\pi$	$+0.20\pm0.12$	$+0.08$	$+0.16\pm0.03$
$K1(1270)$	(1^+)	$G_{V1}/4\pi$	-0.10 ± 0.06	$+0.02$	-0.10 ± 0.02
		$G_{T1}/4\pi$	-1.21 ± 0.33	$+0.17$	-0.54 ± 0.05
$N^*(1440)$	$1(1/2^+)$	$G_{N^*}/\sqrt{4\pi}$	-1.41 ± 0.60		$+0.08\pm0.14$
$N^*(1650)$	$0(1/2^-)$	$G_{N^*}/\sqrt{4\pi}$		-0.04	
$N^*(1710)$	$1(1/2^+)$	$G_{N^*}/\sqrt{4\pi}$		-0.06	
$N^*(1700)$	$2(3/2^-)$	$G^a_{N^*}/4\pi$			$+0.32\pm0.08$
		$G^b_{N^*}/4\pi$			$+0.13\pm0.04$
$N^*(1720)$	$1(3/2^+)$	$G^a_{N^*}/4\pi$			-0.04 ± 0.01
		$G^b_{N^*}/4\pi$			-0.03 ± 0.03
$\Lambda^*(1405)$	$0(1/2^-)$	$G_{\Lambda^*}/\sqrt{4\pi}$		-0.07	
$\Lambda^*(1600)$	$1(1/2^+)$	$G_{\Lambda^*}/\sqrt{4\pi}$			-2.76 ± 0.11
$\Lambda^*(1670)$	$0(1/2^-)$	$G_{\Lambda^*}/\sqrt{4\pi}$	-3.17 ± 0.86		-0.54 ± 0.07

change because their main coupling constants ($g_{K\Lambda N}$ and $g_{K\Sigma N}$) were not subject to SU(3)-symmetry constraints and in fitting data they generate quite small values of both the *t*-channel and $g_{K\Lambda N}$,$g_{K\Sigma N}$ couplings compared to those produced in the AS and SALY fits. The *t*-channel coupling constants come out to be smaller in SALY than in AS. This feature arises since the SALY model includes spin-3/2 baryonic resonances and hence the need for the *t*-channel exchanges is reduced, in line with duality ideas [9]. The role of duality (the interplay between s- and *t*-channel strengths) and its effect on spin observables is discussed in Sec. III A 2.

Can the general rules for spin observables conjectured in FTS and summarized in Sec. II be seen in the dynamical results? What is the behavior of spin observables at lower energies and what role is played by particular baryonic resonances and by kaon exchanges? How do the specific isobar and *t*-channel dynamics of the three models affect spin observables? Are some spin observables particularly sensitive to interesting dynamics and are therefore particularly important to measure? Those questions are addressed in Secs. III and IV.

II. GENERAL RULES REVISITED

The general rules for the 16 observables are described in detail in FTS [4], which also includes the derivation of such observables from a density matrix approach. Here we simply highlight and confront those rules. For convenience, the definition of the 16 observables are recalled in Appendix A.

A. The helicity rules

The Legendre classes of the 16 observables, which are labeled by $\mathscr{S}_0$, $\mathscr{S}_{1a}$, $\mathscr{S}_{1b}$, and $\mathscr{S}_2$ are

$$\mathscr{S}_0(\mathscr{I};\hat{E};\hat{C}_{z'};\hat{L}_{z'}),$$

$$\mathscr{S}_{1a}(\hat{P};\hat{H};\hat{C}_{x'};\hat{L}_{x'}),$$

$$\mathscr{S}_{1b}(\hat{T};\hat{F};\hat{O}_{x'};\hat{T}_{z'}),$$

$$\mathscr{S}_2(\hat{\Sigma};\hat{G},\hat{O}_{z'};\hat{T}_{x'}).$$

These observables, which are defined as the product of the usual spin observable and the cross-section function $\mathscr{I}$, are called profile functions [4]. The profile functions are proportional to bilinear products of amplitudes. [2] In the above list, the first entry in each class is the cross section or a single polarization observable ($\mathscr{I},\hat{P},\hat{T},\hat{\Sigma}$); the others are all double polarization observables, which appear ordered as beam-target ($\hat{E},\hat{H},\hat{F},\hat{G}$), beam-recoil ($\hat{C}_{z'},\hat{C}_{x'},\hat{O}_{x'},\hat{O}_{z'}$); with the last entry in each class being the target-recoil observables ($\hat{L}_{z'},\hat{L}_{x'},\hat{T}_{z'},\hat{T}_{x'}$). The angular dependence of the above observables are determined by expressing the four helicity amplitudes $H_i(\theta)(i=1,\ldots,4)$ in terms of Wigner rotation functions, with θ denoting the produced kaon's center-of-mass angle. It is then simple to deduce that $\mathscr{S}_m$ class observables are to be expanded in the associated Legendre, $P_{\ell m}(\cos\theta)$, functions. Thus, $\mathscr{S}_{1a}$ and $\mathscr{S}_{1b}$ involve sums $\Sigma P_{\ell 1}$, which vary as $\sin\theta$. Hence, $\mathscr{S}_{1a}$ and $\mathscr{S}_{1b}$ vanish at 0° and 180°. Similarly, class $\mathscr{S}_2$ spin observables involve

[2] The class $\mathscr{S}_2$ observables are determined by the real and imaginary parts of the bilinear combination of helicity amplitudes ($\pm H_1^* H_4 \pm H_2^* H_3$); for class $\mathscr{S}_{1a}$ observables by the real and imaginary parts of ($\pm H_1^* H_3 \pm H_2^* H_4$); and for class $\mathscr{S}_{1b}$ observables by the real and imaginary parts of ($\pm H_1^* H_2 \pm H_3^* H_4$). Finally, the class $\mathscr{S}_0$ observables are determined by the four combinations of the magnitudes $\pm|H_1|^2 \pm |H_2|^2 \pm |H_3|^2 \pm |H_4|^2$.

sums ΣP_{ℓ}, which vary as $\sin^2\theta$ and hence vanish more sharply at those "end points." The $\mathscr{S}_0$ class observables are not necessarily zero at the "end points." However, all other spin observables must vanish at 0° and 180°.

Following this helicity amplitude procedure, FTS deduced several rules.

[h1] The observables $C_{z'}(\theta)$ and $L_{z'}(\theta)$, as functions of the scattering angle θ, must have an odd number of sign-changing (SC) nodes, if they are nonvanishing observables.[3]

[h2] The observable $E(\theta)$ can be nodeless or have an even number of sign-changing zeros.

[h3] If the final-state $J \geq 3/2$ amplitudes vanish, then the following relations must hold at all angles: [4]

$$E \approx +1,\ L_{z'} = -C_{z'},\ L_{x'} = -C_{x'},\ P = -H.$$

These conditions are expected to occur near threshold and to rapidly change as the $J=3/2(K^+\Lambda)$ P waves turn on. Note that these observables are nonzero even when the $J \geq 3/2$ amplitudes vanish. These properties follow directly from Eqs. (4.1)–(4.6) of FTS [4], since only H_1 and H_3 vanish if there are no $J \geq 3/2$ amplitudes.[5]

[h4] The Legendre class $\mathscr{S}_{1a}$ profile observables can have no more than $(2J_{\max}-1)$ intervening nodes (i.e., not counting the end-point nodes). Here, $J_{\max}$ is the maximum J value expected at a particular energy. Near threshold, these observables are thus expected to be nodeless, with a node developing as the $J=3/2$ amplitudes turn on, but no more than 2 nodes being possible, until $J>3/2$ states appear. Note that the $\mathscr{S}_{1a}$ class observables are all nonzero even if $J \geq 3/2$ amplitudes vanish.

[h5] The $\mathscr{S}_{1b}$ class observables were expected to be small near threshold, with nodes developing only at higher energies, since the $J \geq 3/2$ amplitudes are expected to be small near threshold and these observables depend on interference between $J=1/2$ and $J \geq 3/2$ amplitudes.

[h6] The $\mathscr{S}_2$ class observables should be small and nodeless at lower energies. These observables also depend on interference between $J=1/2$ and $J \geq 3/2$ amplitudes.

We shall refer to the above statements as FTS rules h1, . . . , h6.

These remarks are summarized in Table II of FTS. One interesting observation is that "if $\hat{C}_{z'}$ or $\hat{L}_{z'}$ assume an even number of intervening zeroes [sic], then at least one of these zeroes [sic] would be of non-sign changing" (NSC) type. This feature, which will be examined in our later comparison with dynamical models, is a consequence of the requirement that both $\hat{C}_{z'}$ and $\hat{L}_{z'}$ have an odd number of SC nodes, which follows from basic parity requirements. Similar remarks can be made about $\hat{E}$, which must have an even number of SC nodes; hence, an odd number of zeros means that there must be an odd number of NSC zeros. Examples of these cases will be discussed later, when bifurcations appear in the nodal trajectory plots.

Since there are only 4 amplitudes for pseudoscalar meson photoproduction, only 7 measurements of the 16 observables are needed to extract unique amplitudes (one overall phase is arbitrary). Some observables provide redundant information and thus one needs to consult the known rules [10] for selecting seven independent experiments. That issue is not considered in this paper, see Ref. [5].

B. The multipole rules

Additional rules concerning spin observables were discussed by FTS, based on the possible truncation of multipole amplitudes. The advantage of expanding the K^+ photoproduction amplitudes into multipoles $E_{\ell}^{\pm}, M_{\ell}^{\pm}$ is that the orbital angular moment, ℓ, of the final $(K^+\Lambda)$ state can be used to reduce the number of amplitudes, based on the existence of a centrifugal barrier. Of course, this truncation does not include the possibility of dynamical effects, which could magnify selected orbital states. For example, a resonance could emphasize a particular partial wave or competing effects could attenuate selected waves. However, it is just the deviation from ordinary centrifugal-dominated behavior of spin observables that we hope will serve as the best indicator of such dynamical effects.

Several additional features of the 16 kaon photoproduction observables were conjectured in FST, based on the suppression of higher orbital angular momentum states. These include the following.

[m1] A cross-section peak at 0° implies that the combination of the P waves defined by

$$\psi_P^{(1)} \equiv 3E_1^+ + M_1^+ - M_1^-$$

(called type-1 splitting) and the S wave amplitude E_0^+ have a relative phase angle of less than 90°; provided that (1) $\ell \geq 2$ amplitudes are negligible and (2) $|\psi_P^{(1)}| \neq 0$. That is, to get a cross-section peak one needs not only P waves to interfere with the S wave multipole, but also the P waves must have a nonzero (type-1) splitting.

[m2] A second type of P-wave splitting is defined by the linear combination of $\ell = 1$ multipoles:

$$\psi_P^{(2)} \equiv 3E_1^+ + M_1^+ + 2M_1^-$$

(called type-2 splitting). If $\ell \geq 2$ waves can be neglected and there are P waves, but they have zero type-2 splitting, e.g., $\psi_P^{(2)} \to 0$, then (1) the spin observable $\hat{T}_{z'} \to 0$ at 90° and (2) $\hat{P}$ and $\hat{\Sigma}$ are zero at all angles.

[m3] The type-2 splitting also leads to the following possible $\hat{P}$ behavior. In order for the final Λ polarization $\hat{P}$ to have nodes, there must be nonzero type-2 P-wave splitting, $\psi_P^{(2)} \neq 0$, and $\psi_P^{(2)}$ must not be collinear with M_1^-, unless $\ell \geq 2$ multipoles contribute significantly. Furthermore, if the type-2 P wave splitting is nonzero and collinear with the

---

[3] When a function passes through zero we call it a node or more explicitly a sign-changing (SC) zero. If it touches zero without passing through zero we also call it a node or a nonsign-changing (NSC) zero.

[4] A sign misprint for E and H in Ref. [4] is corrected here. Also, the $\mathscr{S}_{1a}$ theorem in Sec. IV of FTS is incorrectly stated as having $T=H$ for no $J=3/2$ amplitudes; the corrected version is that $P=-H$, when there are no $J \geq 3/2$ contributions.

[5] The following relations can be used to deduce these rules: $\hat{L}_{z'} + \hat{C}_{z'} = |H_3|^2 - |H_1|^2; \hat{L}_{x'} + \hat{C}_{x'} = -2\ \mathrm{Re}[H_1 H_3^*]; \hat{P} + \hat{H} = -2\ \mathrm{Im}[H_1 H_3^*]$.

E_0^+ multipole, then, in the absence of $\ell \geq 2$ amplitudes, the polarization $\hat{P}$ has a SC node at 90°.

[m4] Based on a scattering length expansion, it was anticipated that $\hat{\Sigma}$ and $\hat{G}$ are small and nodeless near threshold, with nodes developing only if $\ell > 1$ amplitudes contribute.

[m5] The beam-recoil observable $\hat{O}_{z'}$ and the target-recoil observable $\hat{T}_{x'}$ are both zero at all angles, unless there are $\ell \geq 1$ multipoles and the stretched electric and magnetic multipoles are unequal, e.g., $E_1^+ \neq M_1^+$ in magnitude and phase.

[m6] The observables $O_{z'}$ and $T_{x'}$ are both of Legendre class $\mathscr{S}_2$ and are complementary in their nodal behavior, see Eqs. (5.21) and (5.23) of FTS [4]. By complementary we mean that if one tends to have a node, the other does not so tend.

[m7] For $\hat{T}$ and $\hat{F}$ to have SC nodes, type-2 P wave splitting must be nonzero, until $\ell \geq 2$ waves contribute significantly.

[m8] If the Legendre class $\mathscr{S}_{1a}$ observables $C_{x'}$ and $L_{x'}$ have zeros then, as the momentum increases, these zeros tend to be placed symmetrically about 90°.

[m9] Near threshold, the class $\mathscr{S}_0$ spin observable $C_{z'}$ has a SC node at 90°.

[m10] Near threshold, the class $\mathscr{S}_0$ spin observable $L_{z'}$ has a SC node at 90°.

We shall refer to the above statements as FTS rules: m1, . . . ,m10. We are now ready to confront these FST rules with the spin observables found using three different dynamical models.

III. THE DYNAMIC RESULTS

The kaon photoproduction observables are shown for the Adelseck-Saghai (AS) [6], Williams, Ji, and Cotanch (WJC) [7], and SALY [8] models in Fig. 1 for $E_\gamma^{\rm lab} = 0.920$ GeV, and in Fig. 2 for $E_\gamma^{\rm lab} = 1.40$ GeV. The observables versus angle θ, *not* the profile functions, are presented in Figs. 1 and 2. As emphasized in the Introduction, these models are based on selected baryon resonances and exchanged mesons, with the physical basis for these models presented in Refs. [6–8]. Here we simply compare these recent dynamical models with the FTS rules h1, . . . , h6 and m1, . . . , m10.

Note that these plots are organized with observables of a given Legendre classes ($\mathscr{S}_0, \mathscr{S}_{1a}, \mathscr{S}_{1b}, \mathscr{S}_2$) in columns, with the first row giving the cross section and the single spin observables P, T, and Σ. The second row of plots in Figs. 1 and 2 gives the beam-target (E, H, F, G); the third row of plots shows the beam-recoil ($C_{z'}, C_{x'}, O_{x'}, O_{z'}$). The fourth row of plots gives the target-recoil ($L_{z'}, L_{x'}, T_{z'}, T_{x'}$) double spin observables.

To facilitate comparison with the FTS rules, the c.m. nodal angles (in degrees) for the three models are plotted versus the incident photon laboratory energy in Fig. 3. We call these ''nodal trajectory'' plots. These curves have been calculated in the appropriate energy domain for each model, i.e., $E_\gamma^{\rm lab} \leq 1.5$ GeV for AS and $E_\gamma^{\rm lab} \leq 2.1$ GeV for WJC and SALY. The nodal angles are the angles at which a spin variable has a sign-changing (SC) zero. A single node which moves with increasing beam energy appears as a single curve. A bifurcating curve shows the energy evolution of a nonsign-changing zero into two SC nodes (see the observable E for a clear example). These nodal plots are organized by Legendre class and also as single spin observable (top row), double-spin beam-target (second row), beam-recoil (third row), and target-recoil (bottom row). Examination of Figs. 1–3 allows one to confront the three dynamical results with the FTS rules.

A. Helicity rules

The observables of the Legendre class $\mathscr{S}_{1a}, \mathscr{S}_{1b}$, and $\mathscr{S}_2$ are all seen to vanish as expected at the end points (0° and 180°). Only the set $\mathscr{S}_0(\mathscr{T}; \hat{E}; \hat{C}_{z'}; \hat{L}_{z'})$ are nonzero at both of these end-points. Also note that the $\mathscr{S}_{1a,1b}$ class observables approach the end-point angles with nonzero slopes; whereas, the $\mathscr{S}_2$ class observables approach the end-point angles with zero slope. Thus the $\mathscr{S}_{1a,1b} \propto \sin\theta$, and $\mathscr{S}_2 \propto \sin^2\theta$ properties are clearly seen in Figs. 1 and 2.

1. Near and above threshold results

Spin observables for the three dynamical models are now examined at two energies, $E_\gamma^{\rm lab} = 0.920$ GeV and 1.4 GeV for the purpose of testing the FTS rules. The spin observable asymmetries at $E_\gamma^{\rm lab} = 0.920$ GeV, which are near the (γ, K^+) threshold of $E_\gamma^{\rm lab} = 0.911$ GeV, are shown in Fig. 1. The case of $E_\gamma^{\rm lab} = 1.4$ GeV is shown in Fig. 2.

At 0.92 GeV, both $C_{z'}$ and $L_{z'}$ display the anticipated sign-changing nodes, see the FTS rules h1, m9, and m10. The function E is nodeless at low momenta and falls slightly below 1 for all three models, which indicates that only small $J = 3/2$ amplitudes are in effect, see rules h2 and h3. Thus, the FTS suspicion that $E(0°) \approx 1$ is an indication of small $J = 3/2$, aligned P waves is realized near threshold in these models. Note the enlarged scale for the E plot in Fig. 1.

The consequences of assuming small aligned P wave amplitudes, e.g., $L_{z'} = -C_{z'}$ (rule h3), are realized for all three models at 0.92 GeV. For example, we also see that $L_{x'} = -C_{x'}$ and $P(\theta) = -H(\theta)$ in Fig. 1. Thus rule h3 is fully realized near threshold. Indeed, the small deviation from these FTS rules can be used as a measure of the special sensitivity of each spin observable near threshold to $J = 3/2$, aligned P wave amplitudes.

Assuming that at 0.920 GeV the $\mathscr{S}_{1a}$ observables are dominated by $J = 1/2$, Fig. 1 shows that the AS model has $J = 1/2$ amplitudes of the largest magnitude, that the WJC amplitudes are smaller, and the SALY model gives in general the smallest $J = 1/2$ contributions. The $\mathscr{S}_0$ observable E also shows this 1/2 strength pattern. This behavior is consistent with the coupling constants [8] of the three models. Note that the fact that P and H are small compared to $C_{x'}$ and $L_{x'}$ indicates constructive interference between the helicity amplitudes H_1 and H_4, e.g., they tend to be parallel near threshold.

The next FTS rule h4, which is based on general helicity amplitude considerations, concerns the maximum number of nodes for observables in Legendre class $\mathscr{S}_{1a}(\hat{P}; \hat{H}; \hat{C}_{x'}; \hat{L}_{x'})$. For just $J = 1/2$ amplitudes, this class of observables should be nodeless near threshold, which is indeed the case at 0.920 GeV, see Fig. 1. As the $J = 3/2$ amplitudes turn on, due to either aligned P waves ($1 + 1/2 = 3/2$)

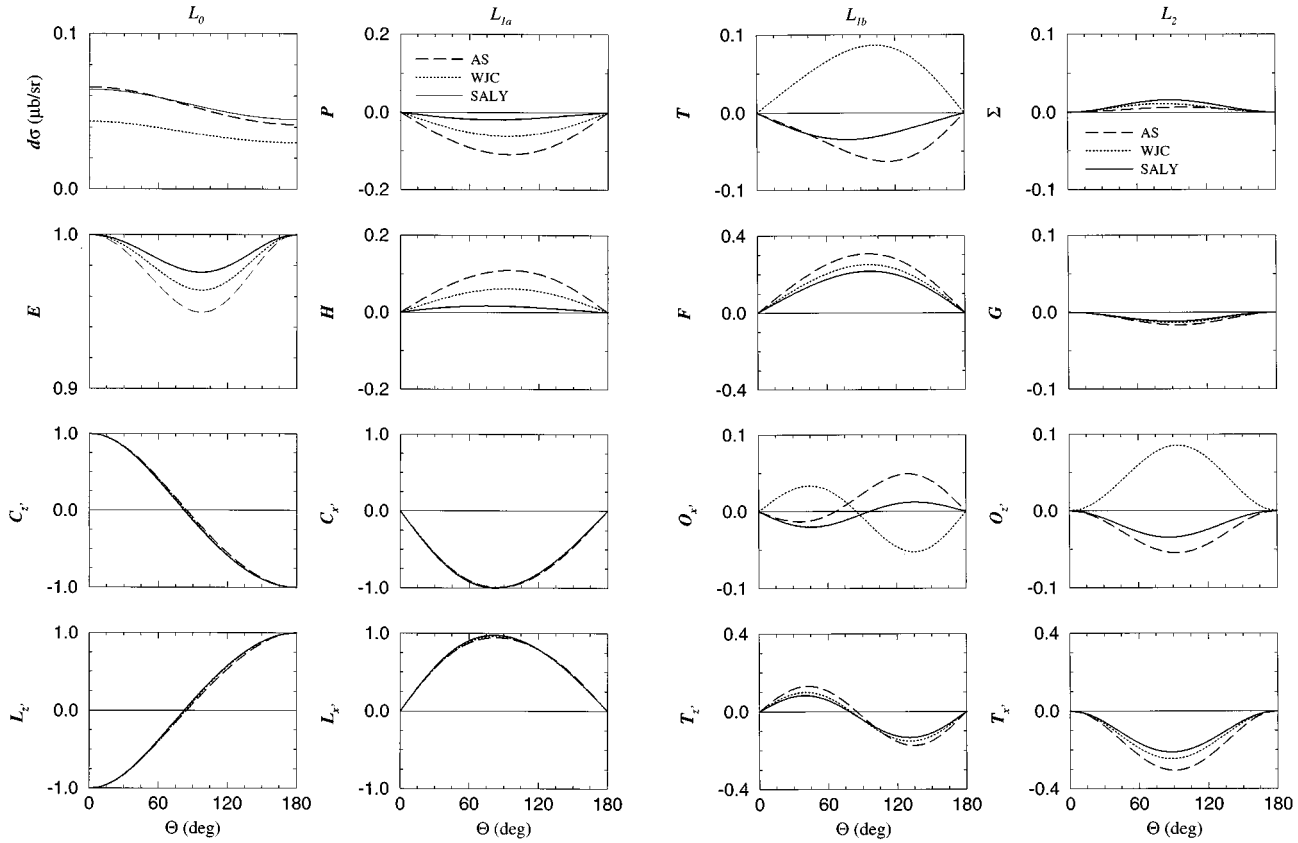

FIG. 1. The 16 observables for kaon photoproduction process $\gamma p \to K^+\Lambda$, for the AS (dashed), WJC (dotted), and SALY (solid) models are presented versus kaon c.m. angle θ in degrees. The photon laboratory energy is $E_\gamma^{\rm lab}=0.920$ GeV, which is just above the kaon production threshold of 0.911 GeV. Observables of Legendre class $\mathscr{L}_0$, $\mathscr{L}_{1a}$, $\mathscr{L}_{1b}$, and $\mathscr{L}_2$ are presented in each column. The first row gives the differential cross section and the single spin observables; the next rows are the beam-target, the beam-recoil, and the target-recoil double spin observables.

or unaligned D waves ($2-1/2=3/2$), the $\mathscr{L}_{1a}$ observables could develop intervening nodes, but not more than two, until the $J>3/2$ states turn on.

Indeed, at 1.4 GeV some $\mathscr{L}_{1a}$ spin observables do develop nodes, see Fig. 2. In particular, the observables P and H, each develop one SC node for the SALY model. For the SALY and WJC models $L_{x'}$ develops two nodes, while for AS, $L_{x'}$ stays at one node at 1.4 GeV. These results comply with the FTS restriction h4 that $\mathscr{L}_{1a}$ observables have no more than two nodes until $J>3/2$ amplitudes are strong. Hence, at 1.4 GeV the $J>3/2$ amplitudes are not explicitly seen in the nodal structure of the $\mathscr{L}_{1a}$ observables. The double nodal structure of $L_{x'}$ is a possible indication of interesting $J=3/2$ dynamics in the proton to Λ spin rotation function ($D_{LS}^{p\Lambda}$, see Appendix A).

For the $\mathscr{L}_{1b}$ observables ($T;F;O_{x'};T_{z'}$) at 0.92 GeV (Fig. 1), two are nodeless (T,F) and two ($O_{x'},T_{z'}$) have nodes in the vicinity of 90°. Thus the node part of rule h5 works for T,F, but not for $O_{x'},T_{z'}$. The $\mathscr{L}_{1b}$ observables depend on interference between $J=1/2$ and $J=3/2$ amplitudes; hence, we can conclude that these $O_{x'},T_{z'}$ nodes near 90° yield important $1/2\times3/2$ interference information for all three models. The reason for these nodes is presented later.

For the $\mathscr{L}_{1b}$ observables at 1.4 GeV (Fig. 2), T acquires one node for WJC and SALY, while the AS model remains nodeless. The observable F stays nodeless for all three models at 1.4 GeV. Double nodes appear in $O_{x'}$ for the SALY and WJC results, while AS stays at one node. The above double nodes seem to be located symmetrically above and below 90°. For $T_{z'}$ SALY gets three, while AS and WJC stay with one node each, near 90° and 0°, respectively. The mechanisms for these changes with energy are more readily understood by examination of the nodal trajectory plots of the next section.

The $\mathscr{L}_2$ observables ($\Sigma;G,O_{z'};T_{x'}$) at 0.92 GeV (Fig. 1) comply with rule h6; they are all nodeless and all, except perhaps $T_{x'}$, are small. These observables, as in the $\mathscr{L}_{1b}$ case, depend on $J=1/2\times3/2$ interference, which is why they are expected to be small near threshold. At 1.4 GeV (Fig. 2), Σ acquires an even number of nodes (2) for AS and WJC, while Σ remains nodeless for SALY. Also G and $O_{z'}$ each acquire one node, but only for the SALY model. The observable $T_{x'}$ remains nodeless at 1.4 GeV for all three models, but with much angular structure. All of these features agree with rule h6. However, the acquisition of an even number of nodes in Σ for some models at and below 1.4 GeV is a surprise, as will be discussed later.

Now let us return to the $\mathscr{L}_0$ observables. At 1.4 GeV (Fig. 2), the $\mathscr{L}_0$ spin observables vary considerably with angle and some have nodes. The rules that $E(\theta)$ must have an even number of nodes (h2) and $C_{z'}$ and $L_{z'}$ an odd number of nodes (h1), are clearly satisfied. However, the three models manage to satify these theorems in different ways, especially in the number of nodes. This suggests that their ''nodal struc-

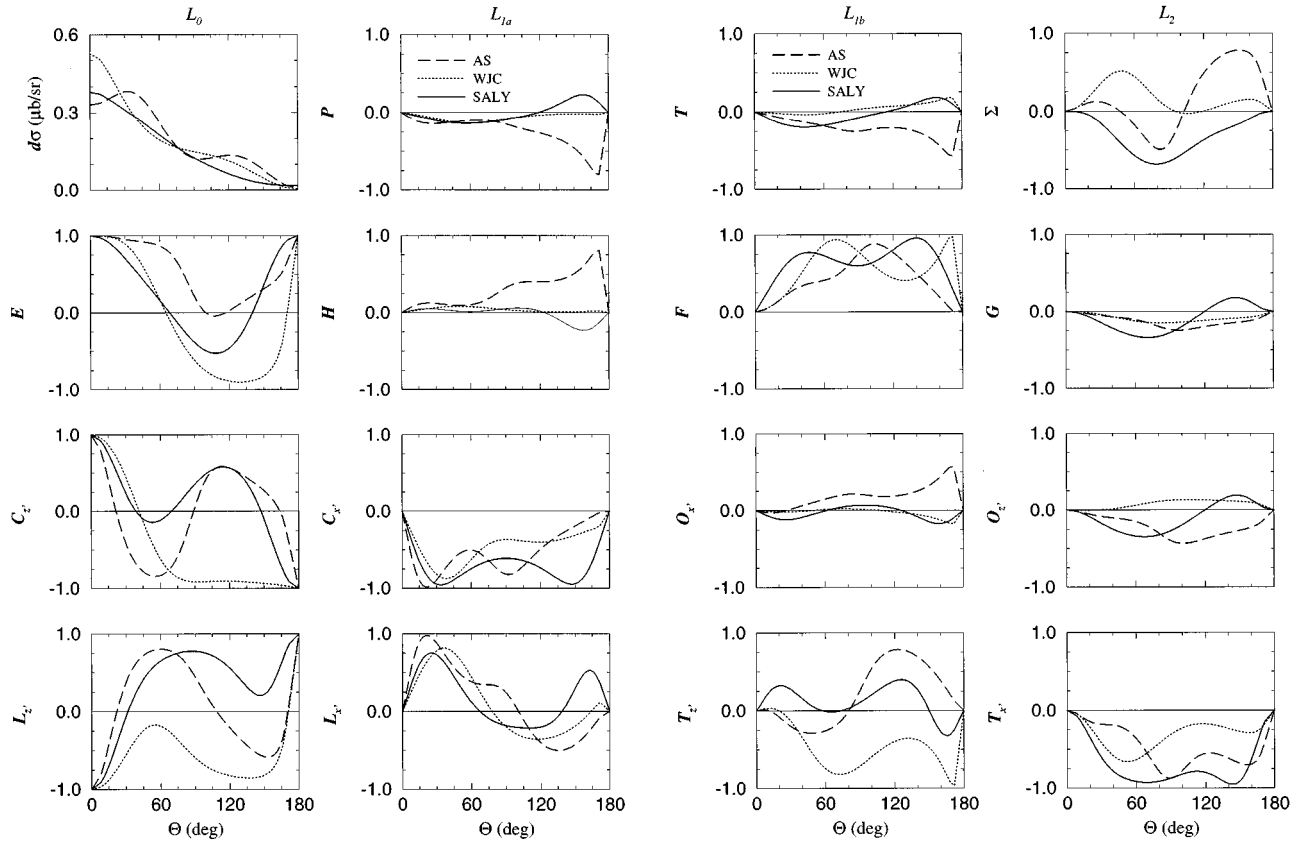

FIG. 2. Same as Fig.1, but for a photon energy of $E_\gamma^{\rm lab}=1.4$ GeV.

ture'' and the evolution of nodes with energy, is a source of specific dynamical information.

All of the models display nodal structures consistent with the h1, . . . , h6 rules. To understand how these nodes develop with increasing energy, and the underlying reasons for the nodal structure of spin observables, it is more convenient to examine ''nodal trajectory'' plots. We shall consider consequences of having a limited number of multipole amplitudes later.

2. Nodal trajectories

To follow the detailed development of nodes with increasing energy we now examine the ''nodal trajectory'' plots of Fig. 3. The nodal angles (e.g., angles at which SC nodes occur) are plotted versus the photon's laboratory energy.

a. Single spin observables. Let us start with the single spin observables ($P,T,$ and Σ), which are presented in the top row of Fig. 3. (The cross section, and hence $\mathscr{T}$, is nodeless.) The recoil Λ polarization, P in Fig. 3, has no nodes for the AS model; one node starting at 180° at 1.47 GeV for the WJC case; and an early node starting at 180° at 0.96 GeV for the SALY model. Both AS and WJC models do not have spin-3/2 resonances, in contrast to the spin-3/2 isobar that is part of the SALY model (see Table I). That isobar accounts for the dramatic difference in the observable P; namely, the early 180° node for the SALY model and the subsequent strong energy dependence of its single node is a reflection of the 3/2, $\ell=1$ resonance $N^*(1720)1(3/2^+)$ at about $E_\gamma^{\rm lab}=1.1$ GeV, corresponding to the total energy of $\sqrt{s}=1.716$ GeV in the center-of mass frame. The other models rely on t channel exchanges for their $J=3/2$ strength at low energies.

Similar reasoning applies to the observable T in Fig. 3, which also has an early 180° node for the SALY model. For WJC, the target polarization T has a node due to $J=1/2^+$ strength, but the node displays smooth nonresonant evolution since the WJC model has no $J=3/2$ resonances. Thus, the nodal structure of P and T are sensitive to explicit s-channel spin-3/2 resonances, but are not so revealing concerning t-channel contributions. The curves P and T for SALY are therefore good examples of resonance-driven nodal trajectories and show how such plots can be used to extract detailed resonance dynamics.

The same SALY-3/2 resonances drive the spin observable H, which has a particularly dramatic nodal trajectory as seen in Fig. 3. This case will be discussed in the beam-target section.

For the photon asymmetry observable Σ the bifurcating behavior seen in Fig. 3 for the AS and WJC models is unexpected. This observable is *not required* to have an even number of nodes. (In contrast, E is restricted to an even number of nodes, which is the reason for its bifurcating nodal trajectory.) *To get two nodes in* Σ*, especially at low energies there has to be some* $J=5/2$ *amplitude strength.* That strength is apparently not due to any 5/2 resonances, since none of the models have explicit $J=5/2$ resonances. Instead, the $J=5/2$ strength at low energies arises from a t channel mechanism

The polarized beam asymmetry Σ shows this unexpected double nodal structure for the AS model at lower energies and at higher energies for the WJC model. For the SALY

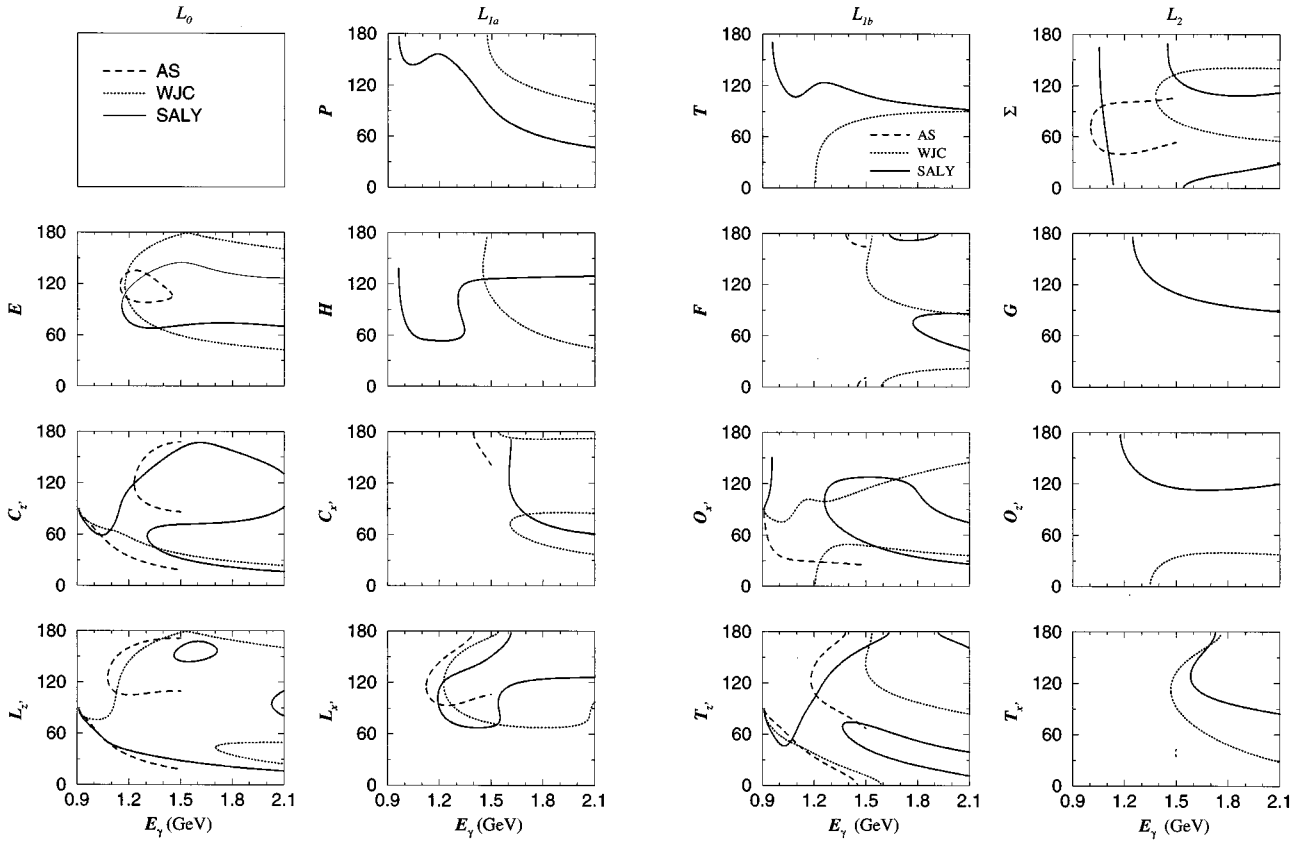

FIG. 3. The nodal trajectory plots for the spin observables of Legendre class: (a) $\mathscr{S}_0$, (b) $\mathscr{S}_{1a}$, (c) $\mathscr{S}_{1b}$, and (d) $\mathscr{S}_2$. The c.m. kaon angle at which a sign-changing zero occurs for a given spin observable is plotted versus the incident laboratory photon energy. The single spin observables are presented in the top row, while the beam-target, beam-recoil, and target-recoil double spin observables are located in the second, third, and bottom rows, respectively. Again the curves are displayed as AS (dashed), WJC (dotted), and SALY (solid).

model, a single node appears at 180° and moves rapidly to 0°; two nodes appear at higher energy and evolve smoothly. In the region that SALY has one node, this single node and its rapid motion can be accounted for by its $J=3/2$ resonances. The double node at higher energy for SALY occurs when it picks up $J=5/2$ strength, probably from t-channel effects. The general form of the $\hat{\Sigma}$ observable is $\sin^2\theta(a+b\cos\theta+c\cos^2\theta)$, where the terms a and b arise from interference between $J\geqslant 1/2$ states, while the term c arises only if $J\geqslant 5/2$ states contribute; for example, c arises first from a $3/2\times 5/2$ amplitude interference. Therefore, to get the double nodal structure seen for the AS model near threshold, one needs a sizable c term or, equivalently, at least $J=5/2$ multipoles. It is also clear from this general form that for small 5/2, but sizable 3/2, amplitudes, the term b arises first from interference between $3/2\times 3/2$ and hence can give only one node.[6]

The $J=5/2$ amplitudes could arise from a mechanism that boosts the orbital angular momentum to higher values. The striking of a virtual P-wave meson by a polarized incident photon (t-channel exchange) provides such a mechanism. For example, if a virtual K^+or K^* kaon peals off from the nucleon in a P wave, it can receive an extra orbital angular momentum boost when it is struck by the incident photon. The kaon then boosts to an $\ell=2$ state, which, when added to the Λ's 1/2 spin, generates $5/2^-$ and $3/2^-$ strength, even at low energies, without an explicit 5/2 baryon resonance. Thus, we learn that t channel, or kaon exchange provides $5/2^-$ and $3/2^-$ strength and therefore contributes to the $(E_2^+, M_2^+)5/2^-$ and $(E_2^-, M_2^-)3/2^-$ multipoles.[7]

This mechanism is illustrated in Fig. 4. The AS model has particularly strong t-channel couplings, which are generated, in a duality sense, to make up for the absence of the 3/2 resonances contained in the SALY model. The WJC model, which has weaker coupling in the t-channel processes, does ultimately also reveal a similar bifurcation in the Σ observ-

[6]To generate n SC nodes, an observable needs to be described as $\sin^m\theta$ times a polynomial of order n in $\cos\theta$. Here $m=0,1,2$ depending on the Legendre class $\mathscr{S}_m$.

[7]In principle, all u and t channel resonances contribute to all multipoles. However, for the dynamical models considered here some higher multipoles receive their major contribution from t-channel exchange (see Fig. 4), in line with the duality hypothesis. This behavior was determined by numerical investigation of these dynamical models (see also Sec. III B). For example, for the simplest model (AS), the $l=2$ to 4 multipoles are changed most dramatically when t-channel resonances are omitted, than when we dropped individual u and t channel terms from the AS model and then fitted the same database and extracted the corresponding $l=0$ to 4 multipoles.

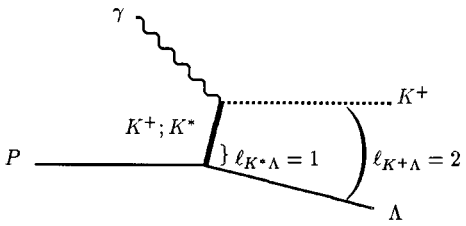

FIG. 4. The *t*-channel or kaon exchange mechanism. The virtual kaon (K^+ or K^*) is typically emitted in a P wave. The incident photon can boost the virtual kaon to a $\ell_{K^+\Lambda}=2$ state. Then the final-state angular momentum is obtained by adding in the Λ spin as $\vec{2}+\vec{1/2}\rightarrow 3/2^-,5/2^-$; the negative parity arises from the rule $(-1)^{\ell}$. This mechanism feeds into the $(E_2^- M_2^-)3/2^-$ and $(E_2^+ M_2^+)5/2^-$ multipoles. It is also possible for the incident photon to lower $\ell_{K^+\Lambda}$ to zero, which could affect the $E_0^+ 1/2^-$ amplitudes; this multipole is already large so the major effect is the one illustrated here. If the kaon is left in a P wave after the photon is absorbed, then the above *t* channel can contribute to the $3/2^+ M_1^+$ and $1/2^+ E_1^-, M_1^-$ states; however, these multipoles are usually dominated by *s* channel contributions. If the virtual kaon is the $K1$, it is produced mainly in an S wave and therefore yields $\ell_{K^+\Lambda}=1,0$, or $J=1/2^+,3/2^+$ or $1/2^-$ states, which are usually dominated by *s*-channel contributions.

able, but not until higher energies of about 1.4 GeV.

Although the SALY model has stronger *t*-channel strength than does the WJC model (see Table I), it does not display the bifurcation one might expect, because even at low energies the $J=3/2$ resonances play a non-negligible role. For the SALY model the above role for *t*-channel $J=5/2$ amplitudes is not seen. Instead, in Fig. 3, the Σ for SALY has a 180° node which travels rapidly toward 0° in the region of the $J=3/2$ resonances of this model. This property is related to the resonance-driven evolution of the single node in the observables P, T, and H for the SALY model. In the Σ case, the 3/2 resonance increases the size of the $b\cos\theta$ term and the rapid variation of b with energy and its sign change explain how the 3/2 resonance causes the rapid $180°\rightarrow 0°$ nodal evolution. At higher energies the SALY model does acquire 5/2 strength and thus a nonzero quadratic term, $c\cos^2\theta$, permits the appearance of two nodes, as seen in Fig. 3. Thus, all of the Σ curves arise from resonance and/or *t*-channel mechanisms.

We conclude that the observable Σ provides a particularly sensitive test of resonances and of $J=5/2$ amplitudes and thereby of *t*-channel or meson exchange processes. The basic idea of duality, which equates a sum over all *t*-channel processes with a sum over all *s*-channel resonances, shows that there is a close relationship between a dynamical model's content with respect to assumed resonances and the corresponding strength of the *t*-channel exchanges needed to fit the data. Thus, another way to describe the significance of Σ is that it tests the duality structure of the dynamics. This result and the enhanced role of $J=5/2$ amplitudes were not anticipated by FTS.

b. Beam-target spin observables. We now discuss the nodal trajectories for the beam-target observables, which are given in the second row of Fig. 3. For the observable E, a bifurcation of nodes appears in Fig. 3. Recall that E is restricted to an even number of nodes by rule h2. Therefore, if a (NSC) zero develops in this observable and with increasing energy this vanishing extremum acquires a nonzero value, then it must produce two SC nodes: that is what we mean by a bifurcation. Insight into this rule is gained by noting [4] that $\hat{E}$ has the form $a+b\cos\theta+c\cos^2\theta$. The coefficient c is determined by amplitude products of the form $3/2^+\times 3/2^+$ and interferences $1/2^+\times 3/2^+$. Thus c can exist either by having a 3/2 resonance (as in SALY) or by enhanced *t* channel 3/2 strength, without invoking 5/2 terms. Hence, the quadratic form can be realized for those two reasons by all models. Indeed, all models (Fig. 3) display a bifurcation at about the same photon energy; for AS and WJC the term c is generated by the kaon exchange process; whereas, for the SALY case it is generated by the underlying 3/2 resonances. There are no nodes in E until about 1.2 GeV, even though the $a+b\cos\theta$ would seem to allow for low energy nodes. However, the a term is dominated by $|E_0^+|^2$, while b depends only linearly on E_0^+'s interference with $\ell=1$ multipoles. Thus, the a term dominates and without a sizable contribution from $b\cos\theta$, single nodes are prevented and one goes directly to double nodes at higher energies.

The beam-target observable H is related to the single spin observable P which was discussed in the previous section. The rapid variation of the nodal location of H for the SALY model is due to the 3/2 resonance, but in a more dramatic fashion than for P, see Fig. 3. Thus the double spin observable H has enhanced 3/2-resonance dependence. This is another good example of nodal structure generated by resonances. The relation between the nodal trajectories for P and H is particularly instructive. We know that $\hat{P}+\hat{H}=-2\ \mathrm{Im}(H_1 H_3^*)$, where the H_1 and H_3 helicity amplitudes are zero unless $J\geq 3/2$ amplitudes exist. Thus, in the absence of $J\geq 3/2$ amplitudes, we recover the theorem $P=-H$ of rule h3. In the case of the two $J=3/2$ SALY resonances, the difference between P and H is determined by $\mathrm{Im}(H_1 H_3^*)$ and therefore by the associated amplitudes interference. The two SALY resonances drive both P and H in a very revealing manner. Note that for the WJC model there are no $J=3/2$ resonances and consequently nodes for that case develop at higher energy and move from 180° to smaller angles smoothly for both P and H. This is an example of a nonresonant driven nodal evolution, where the $J=3/2$ strength probably arises first from *t*-channel effects.

Hence, observation of both P and H could reveal the presence or absence of resonance dynamics. One would need to measure the polarization of the final Λ via its decay and also measure H which requires a linearly polarized photon plus a proton target polarized in the $\hat{x}$ direction. In the present case we are dealing with two nearby $J=3/2$ resonances albeit of different parity; it would be of interest to explore the nature of nodal trajectories for isolated and/or dominant resonances such as are thought to occur in η meson production [11].

For F we see no nodes until higher energies (above 1.4 GeV) for all models. The AS develops two nodes, followed by WJC with two nodes, and then SALY comes on with three nodes in the 1.8 GeV region. This is clearly not driven by any of the resonances, they occur at lower energies. The form of F is $\sin\theta(a+b\cos\theta+c\cos^2\theta+d\cos^3\theta)$, where from Eq. (D6) of FTS the a term is enhanced by the large E_0^+

multipole, which makes it difficult for the b and c terms, needed to generate nodes, to play a role. But this amplification of the a term is also true for the observables P and T and they do exhibit nodes; whereas, for F there is a delay in the appearance of nodes. The b term for F must therefore conspire to be smaller than for these earlier cases; it might be characteristic of the observable F not to have nodes only after a critical energy is reached. When double nodes do turn on in F for the AS model, it is because a and c are comparable; we need to invoke $\cos^2\theta$ terms to get double nodes. To generate c, the AS model must use its considerable 5/2 amplitudes, so again this suggests a t-channel mechanism. The same reason explains the later appearance of two nodes for the WJC model, which is weakest in t-channel strength. The SALY model is the first to develop three nodes in F, which means the d term is effective, but not until higher energies where $J \geqslant 5/2$ strength can be generated in several ways.

The observable G has a single node for only the SALY model, as seen in Fig. 3. This observable is of the form $\sin^2\theta(a+b\cos\theta)$, where a depends on P-wave interferences of the type $(1/2^+ \times 3/2^+ + 3/2^+ \times 3/2^+)$, and also S- and D-wave interferences. The b term, which is needed to generate a single node, depends on P- and D-wave interference; indeed, in b the D waves ($5/2^-$ and $3/2^-$ multipoles) appear multiplied by P-wave amplitudes ($3/2^+$ and $1/2^+$ multipoles). Even above the resonance region, P-wave amplitudes ($3/2^+$ and $1/2^+$) interfere with D waves sufficiently to generate a b that is comparable to a only for the SALY model, which yields the single node in G seen in Fig. 3. For the AS and WJC models, the b term does not have sizable P-D wave interference; also, the S- and D-wave interference keeps a large enough, due to large S waves, to make it difficult in general to generate nodes in G. A single node in G provides evidence for significant P-D wave interference and possible P-wave enhancement.

In many cases, especially at low energies, nodal trajectories are seen to reveal either resonance or t-channel effects, and/or enhancements due to dominance of the $\ell = 0$ multipole.

c. Beam-recoil spin observables. Now consider the nodal trajectory plots for $\hat{C}_{z'}, \hat{C}_{x'}, \hat{O}_{x'}, \hat{O}_{z'}$.

At first glance, $\hat{C}_{z'}$ in Fig. 3 seems impossible to understand, but it does have some simple features. All models have a 90° node near threshold. This property can be understood from the general form for this observable $\hat{C}_{z'} = a + b\cos\theta + c\cos^2\theta + d\cos^3\theta$, where near threshold b is dominated by $|E_0^+|^2$, while a depends linearly on E_0^+'s interference with $\ell = 1$ multipoles. Thus near threshold the $\cos\theta$ term dominates and gives the 90° node near threshold. The SALY-3/2 resonances show up in $C_{z'}$ by rapidly moving that 90° node first to smaller and then to larger angles. In the general form of the observable $\hat{C}_{z'}$ the cubic term $d\cos^3\theta$, appears even when a truncation to $\ell \leqslant 1$ is used. The d term involves interference between the aligned $J = 3/2$ amplitudes. Therefore, in addition to explaining the rapid motion of the lower energy node by 3/2 resonances, at ≈ 1.31 GeV there is enough off-resonant 3/2 strength in the SALY amplitudes to invoke the cubic term and hence yield the three nodes seen in Fig. 3. Similarly, at $\approx$ 1.23 GeV the AS model has considerable 3/2 strength, not by a resonance, but by t-channel enhancement. Thus, it exhibits a smooth (nonresonant) evolution of its low energy node, followed by an early turn-on of three nodes. This early turn-on of 3/2 amplitude appeared earlier in the bifurcations seen in Σ and E. For WJC, there are only small 3/2 amplitudes (it has no 3/2 resonances and its kaon exchange is small); therefore, it exhibits a smooth evolution of the 90° node toward zero angle,

For $\hat{C}_{x'}$(Fig. 3) we note an absence of nodes until energies above 1.4 GeV. The AS and then the SALY model exhibit one simple node, while WJC turns on with three above 1.61 GeV. The prevention of early nodes is understood from Eq. (D9) of FTS, wherein the leading $\sin\theta \times a$ term is dominated by the S-wave multipole $|E_0^+|^2$.[8]

The spin observable $\hat{O}_{x'}$ has a complicated nodal structure that can be understood from its general form $\hat{O}_{x'} = \sin\theta(a + b\cos\theta + c\cos^2\theta)$, where near threshold b is dominant since it depends linearly on E_0^+'s interference with $3/2^+$ multipoles; whereas, a involves only $\ell \geqslant 1$ waves. Thus a 90° node near threshold occurs for all three models, which although not required by FTS rules, arises from dynamical dominance of S waves near threshold. That node moves most rapidly for the SALY model, due to its 3/2 resonances; the SALY model is also able to turn on the c term to generate two nodes above 1.26 GeV due to off-resonance $3/2^+$ strength. The AS model displays a smooth evolution of the low energy 90° node because it lacks a 3/2 resonance. The WJC exhibits structure in the evolution of its 90° node and also acquires two nodes above 1.2 GeV. This WJC evolution arises perhaps from the energy dependence of the S-wave amplitude and the onset of $3/2^+$ strength and interference with $1/2^+$ amplitudes

For $\hat{O}_{z'}$, only SALY and WJC exhibit single and smoothly evolving nodes. Its general form $\hat{O}_{z'} = \sin^2\theta(a + b\cos\theta)$, has a dominant because it involves the S-wave E_0^+ multipole, which accounts for the delay in the onset of nodes, which do occur when the $3/2^+$ P waves allow b to compete with a.

d. Target-recoil spin observables. Now consider the nodal trajectory plots in Fig. 3 for $\hat{L}_{z'}, \hat{L}_{x'}, \hat{T}_{z'}, \hat{T}_{x'}$.

For $\hat{L}_{z'}$, recall that FTS h3 indicates that $L_{z'} = -C_{z'}$ if $J \geqslant 3/2$ amplitudes vanish. Similar nodal structure for these two observables is then expected for models with small 3/2 amplitudes; this holds true for the AS case and, to a lesser extent, for the WJC model.

For $\hat{L}_{x'}$, the S wave dominance of the $\sin\theta \times |E_0^+|^2$ term prevents low energy nodes. By the time P waves enter they are strong enough to invoke quadratic terms and generate double nodes; hence the bifurcation for all nodes is seen. This is similar to the E case, except there is no even node $\hat{L}_{x'}$ theorem.

The form of $\hat{T}_{z'}$ is $\sin^2\theta(a + b\cos\theta + c\cos^2\theta)$; we have another case where the S-wave dominance of the b term produces 90° nodes for all models near threshold, followed by a rapid variation for the SALY case due to its 3/2 resonance.

[8]Several such cases occur where the multipole $|E_0^+|^2$ dominates the a and E_0^+ enters linearly in the $b\cos$ terms in the polynomial. That structure prevents nodes until higher energies.

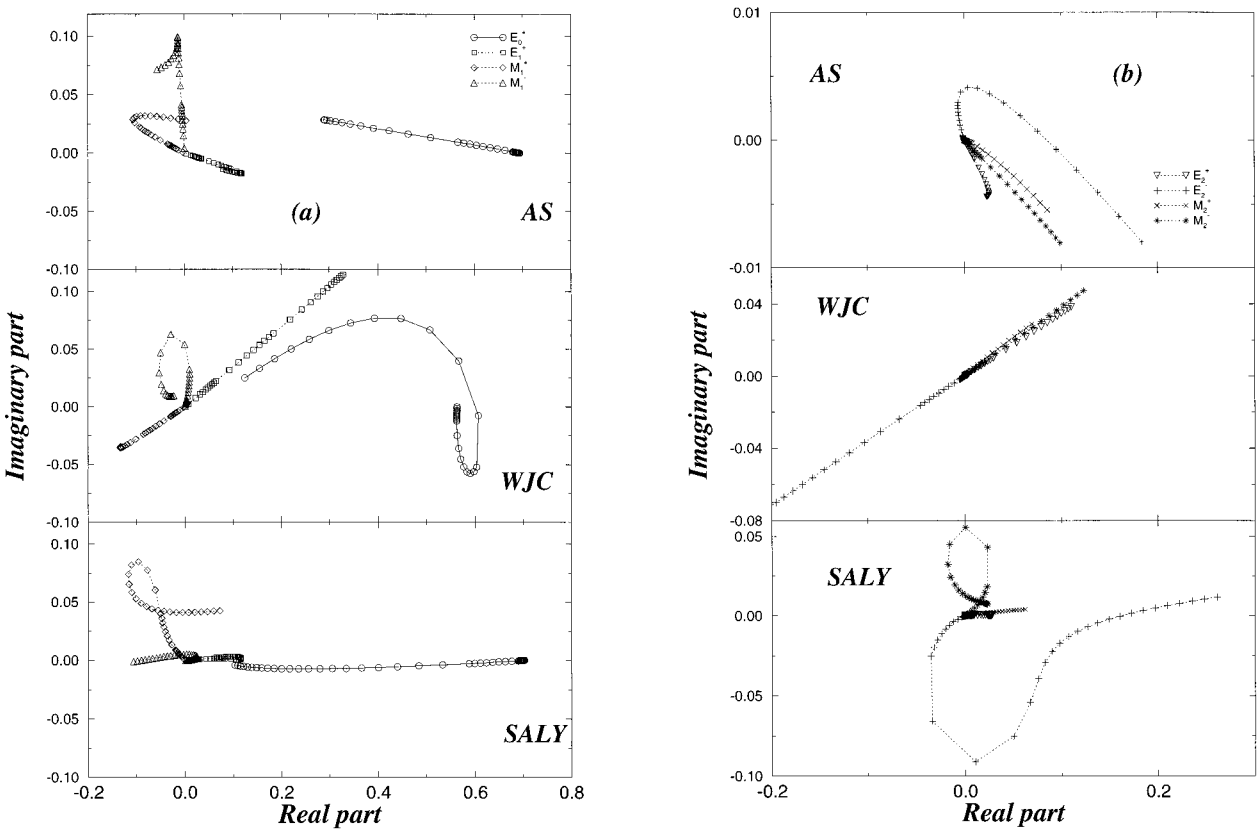

FIG. 5. Argand plots of the electric and magnetic multipoles for the AS, WJC, and SALY models for (a) $\ell \leq 1$ and (b) $\ell = 2$. The S-wave multipole E_0^+ starts at a nonzero point along the real axis and then evolves with energy. All other multipoles start at the origin and follow the trajectories shown as energy increases. For resonant states the Argand plot exhibits the usual looping. The scale in (a) is kept fixed, but it varies with model in (b). Note the role of these amplitudes in observables is typically weighted by $2J+1$ factors; hence D-wave effects can be magnified.

Once the 3/2 amplitudes turn on at higher energies, in part from t-channel effects, then the c term enters and double nodes appear. This is similar to the $C_{z'}$ case.

Finally, with the form $\hat{T}_{x'} = \sin^2\theta(a + b\cos\theta)$ the S wave makes a dominant and nodes are therefore postponed until high energies (1.5 GeV) for WJC and AS (just barely seen, since this is the end of its region) and at 1.55 GeV for the SALY model.

Many of the characteristics described above are determined by the dominance of S waves and the subsequent appearance of P waves. The most interesting cases are those that arise from isobar resonance and/or t-channel effects.

B. Multipole rules revisited

Each multipole includes reference to the final $K^+\Lambda$ orbital angular momentum. Hence, explicit truncations are suggested and additional rules m1, . . . , m10 can be deduced for observables near threshold. The assumption involved in deducing these additional rules is that centrifugal barrier suppression of amplitudes dominates the dynamics, and that resonance or other special dynamic effects can be neglected. However, dynamical models do include baryon resonances and particular t-channel exchanges and therefore it is expected that the FTS m1, . . . , m10 rules will be broken. In contrast, the helicity rules based on general symmetry principles are not and should not be broken.

To facilitate comparison of the dynamical results of AS, WJC, and SALY to the rules offered by FTS, it is best to examine the Argand plots of multipoles (Appendix B) for the AS, WJC, and SALY models. The S- and P-wave multipoles are displayed in Fig. 5(a), while the D waves are in Fig. 5(b). Note the scale is fixed in Fig. 5(a), but varies with model in Fig. 5(b) with the AS having the smallest scale. For convenience, the multipoles are phase rotated to give a real E_0^+ multipole at threshold. Only that S-wave multipole is nonzero at threshold; all others start at zero and evolve as q^ℓ, where q is the $K^+\Lambda$ linear momentum. The WJC model displays a rapid variation in E_0^+ due to its $N^*(1650)1/2^-$ isobar (see Table I); the two other models have E_0^+ multipoles that decrease without resonance (counterclockwise looping) structure. Structure due to the $N^*(1710)1/2^+$ of WJC is seen in the energy evolution of its M_1^- multipole, with all of its other multipoles evolving nonresonantly. The AS displays M_1^- structure from its $N^*(1440)1/2^+$ isobar. The M_1^+ multipole has nonresonant structure in the AS model. For the SALY case, that multipole displays resonance looping due to the added $N^*(1720)3/2^+$ isobar, which also introduces some E_1^+ structure in the SALY model. The SALY model's M_1^- also acquires resonant structure apparently due to its $\Lambda^*(1600)$.

TABLE II. The multipoles for the three models listed in order of their maximum size from threshold to the maximum energy range of the corresponding model, based on Fig. 5. The boldfaced multipoles display counterclockwise resonance looping. The multipoles marked by a dagger receive strength from *t*-channel exchange.

AS	$E_0^+(1/2^-)$	$\boldsymbol{M_1^-(1/2^+)}$	$E_1^+(3/2^+)$	$E_2^-(3/2^-)^\dagger$	$E_2^+(5/2^-)^\dagger$
			$M_1^+(3/2^+)$	$M_2^-(3/2^-)^\dagger$	$M_2^+(5/2^-)^\dagger$
WJC	$\boldsymbol{E_0^+(1/2^-)}$	$E_1^+(3/2^+)$	$\boldsymbol{M_1^-(1/2^+)}$	$E_2^+(5/2^-)^\dagger$	
		$E_2^-(3/2^-)^\dagger$	$M_2^-(3/2^-)^\dagger$	$M_2^+(5/2^-)^\dagger$	
			$M_1^+(3/2^+)$		
SALY	$E_0^+(1/2^-)$	$\boldsymbol{M_1^+(3/2^+)}$	$\boldsymbol{M_1^-(1/2^+)}$	$\boldsymbol{M_2^-(3/2^-)}$	$M_2^+(5/2^-)^\dagger$
			$\boldsymbol{E_1^+(3/2^+)}$		$E_2^+(5/2^-)^\dagger$
			$\boldsymbol{E_2^-(3/2^-)}$		

The D-wave multipoles [Fig. 5(b)] are quite different for the three models. Only the SALY model has explicit D-wave isobars and consequently that model displays resonant M_2^- and E_2^- $3/2^-$ looping. The $5/2^-$ multipoles (E_2^+, M_2^+) evolve smoothly from zero. The small AS D-wave multipoles have some interesting structure, which does not arise from explicit D-wave isobars. For the WJC model, there are no D-wave resonances and the multipoles evolve without structure. Note that the *t*-channel mechanism illustrated in Fig. 4 feeds mainly into the $3/2^-$ and $5/2^-$ multipoles. Thus, aside from the SALY case, these D wave multipoles are connected to that mechanism.

The main properties of the Argand plots of Fig. 5 are the relative strengths of the $\ell \leqslant 2$ multipoles and their relation to their input resonances and the strength of their *t*-channel mechanisms. The $\ell = 0$ multipole E_0^+ is naturally dominant near threshold. It decreases smoothly for the SALY and AS models, but due to the isobars in the WJC model, their E_0^+ multipole has a rapid looping at low energies. Several characteristics are worth noting.

In the AS model: (1) the $(E_0^+)1/2^-$ multipole is driven by the nucleon *s*-channel term and a $\Lambda(1670)$ resonance; (2) the $(E_1^+, M_1^+)3/2^+$ multipoles are not driven by a resonance nor by *t*-channel exchange; (3) the $(M_1^-)1/2^+$ multipole is driven by one $N(1440)$ resonance; (4) the $(E_2^-, M_2^-)3/2^-$ multipoles are driven by *t*-channel exchange; (5) The $5/2^-$ multipoles (E_2^+, M_2^+) receive *t*-channel contributions.

In the WJC model: (1) the $(E_0^+)1/2^-$ multipole is driven by the nucleon *s*-channel term and the $\Lambda(1405)$ plus $N(1650)$ resonances; (2) the $(E_1^+, M_1^+)3/2^+$ multipoles are not driven by a resonance nor by *t*-channel exchange; (3) the $(M_1^-)1/2^+$ multipole is driven by one $N(1710)$ resonance; (4) the $(E_2^-, M_2^-)3/2^-$ multipoles are driven by *t*-channel exchange; (5) the $5/2^-$ multipoles (E_2^+, M_2^+) receive *t*-channel contributions.

In the SALY model: (1) the $(E_0^+)1/2^-$ multipole is driven by the nucleon *s*-channel term and by the $\Lambda(1670)$ resonance; (2) the $(E_1^+, M_1^+)3/2^+$ multipoles are driven by $N(1720)$ resonance; (3) the $(M_1^-)1/2^+$ multipole is driven by the two $N(1440), \Lambda(1600)$ resonances; (4) the $(E_2^-, M_2^+)3/2^-$ multipoles are driven by an $N(1700)$ resonance and by *t*-channel exchange; (5) the $5/2^-$ multipoles (E_2^+, M_2^+) receive *t*-channel contributions.

Using these Argand diagrams we can now discuss the FTS multipole rules. The cross-section peaking rule of FST, under the neglect of $\ell = 2$, requires that $\psi_P^{(1)}$ and E_0^+ be within 90° when viewed as vectors in the complex plane. When one plots $\psi_P^{(1)}$ and compares it to E_0^+, it is seen that rule m1 holds true. Although many FTS multipole speculations do not occur because of the *t*-channel mechanism, rules m9 and m10 are true at low energies, since E_0^+ dominates and $C_{z'}$ and $L_{x'}$ do have SC nodes at 90°. Other rules that hold true are m6, which does get realized in the complementary nature of the nodes; namely, $O_{z'}$ has, while $T_{x'}$ does not have nodes at least below 1.5 GeV. The other FTS multipole rules are not realized, because the FTS truncation assumptions did not take into account that *t*-channel exchange can introduce higher J amplitudes.

Using Fig. 5 we can classify the relative roles of the multipoles for each model. For the three models, the relative importance of the multipoles, based on the maximum size of the multipole over the full energy range, is given in Table II. The resonant multipoles and those that receive strength from *t*-channel exchange are also indicated. The enhanced role for D waves is generated by one or another of these mechanisms depending on the dynamics of the model.

These multipole strengths are consistent, of course, with the driving resonances and the *t*-channel strengths of each model.

The big surprise for FTS is the importance of $\ell = 2$ multipoles in the $3/2^-$ and $5/2^-$ states, due to kaonic exchanges.

IV. SUMMARY AND CONCLUSIONS

Based on general symmetry requirements, FTS [4] deduced general rules for the 15 spin observables in the photoproduction of pseudoscalar mesons. These rules, supplemented by assumptions of smooth energy evolution and centrifugal barrier dominance can be used to define the ''normal'' behavior of spin observables. Deviation from some of these rules indicate a serious violation of a symmetry, such as parity violation. Deviations due to nonsmooth energy evolution, or dominance of selected states, are of dynamical origin, as in the case of underlying hadronic resonances. As a prelude to analysis of future experimental results we have confronted the FTS analysis with three current models [6–8]

of the photoproduction of K^+ mesons.[9]

All of the predictions based on parity and angular momentum conservation are realized in these models, including statements about the even or odd number of sign-changing nodes. The only deviations noted are those possibly attributed to special dynamics, such as underlying resonances. Indeed, an important conclusion is that observation of the nodes of spin observables, as they unfold with energy, offers a powerful way to extract specific dynamical resonance information.

This conclusion is realized by addressing two crucial questions: *(1)* what can the nodal structure of the *forthcoming polarization data* reveal about the highest spin of the intermediate state baryonic resonances required by the reaction mechanism?: *(2)* in *dynamical models*, how can we disentangle the contributions due to genuine baryonic resonances from those mimicked by the kaonic exchanges in line with the duality hypothesis?

To summarize our findings, and in view of the envisioned polarization measurements [1–3] we single out our most significant results on the reaction mechanism deduced by confronting the FTS rules with specific models.

The $\Lambda-$polarization asymmetry is technically the easiest to measure. Here, the nodal structure of P (and also T) is mainly of resonance-driven nature and hence is sensitive to *explicit s*-channel spin-3/2 resonances. The beam-asymmetry Σ proves to be an appropriate observable in testing the validity of the *duality hypothesis* in the strangeness sector. This duality hypothesis is verified by investigating the underlying dynamics of three models; wherein, 5/2 amplitude strength influences spin observables via $3/2\times5/2$ and/or $5/2\times5/2$ interference, even though explicit 5/2 resonances are not included in the models. The 5/2 strength arises from *t*- rather than from *s*-channel dynamics. The beam-asymmetry observable is also very suitable in investigating the role of *explicit* spin-5/2 resonances in the reaction mechanism.

The beam-recoil asymmetries are found very attractive mainly with respect to their sensitivity to $J=3/2$ resonances. The richest information is embedded in the $C_{z'}$ observable, obtained using a circularly polarized beam. The odd number of its nodes are produced through *different* and *distinguishable* mechanisms according to the dynamical ingredients of the models, e.g., the explicit presence of spin-3/2 resonances versus the manifestation of the duality through the *t*-channel exchanges. This property is also true for the beam-target observable E. In addition, the cubic term in $\cos\theta$ arises through the 3/2 amplitudes interferences. The other beam-recoil observable ($C_{x'}$) with circularly polarized beam shows high sensitivity to the $J=3/2$ aligned P waves producing an *explicit* signal for the $J=3/2$ resonances. The asymmetries $O_{x'}$ and $O_{z'}$ corresponding to a linearly polarized photon beam contain important information on $1/2\times3/2$ interferences. Even at low energies, the $O_{x'}$ observable shows deviations from FTS rules for the three models because of *dynamical* effects.

The next double polarization family, beam-target, contains some common features with the above asymmetries. Namely, the observables connected to the circularly polarized beam, E and F, have behavior comparable to $C_{z'}$ and Σ, respectively. For the linearly polarized beam observables the situation is slightly different. The H asymmetry manifests characteristics similar to those of P, with *s*-channel spin-3/2 resonance effects amplified because of an enhancement due to a large E_0^+ multipole in the $\cos\theta$ term, while the nonresonant driven nodal structure due to duality induces a very different evolution. The G asymmetry is driven by a spin-rich interference between 1/2, 3/2, and 5/2 terms. Hence, the appearance of a single node in this observable provides evidence for significant $P\times D$ wave interference and possible P wave enhancement.

The last set of observables, target-recoil asymmetries, are characterized by the dominance of S waves and the subsequent appearance of P waves arising from isobar resonance and/or *t*-channel effects, similar to the cases seen already for observables within other families. This redundancy in information content is of course expected [10] from analysis of the number of independent experiments.

Nodal angle versus E_γ trajectories, based on *direct experimental information*, rather than specific dynamical models, should provide a powerful tool in pinning down the reaction mechanism of the strangeness electromagnetic production processes and, hopefully, in the search for missing resonances [14].

ACKNOWLEDGMENTS

We wish to thank Dr. C. Bennhold, Dr. J. C. David, Dr. S. A. Dytman, Dr. R. A. Eisenstein, Dr. C. Fayard, Dr. G. H. Lamot, and Dr. F. Piron, for their help and encouragement. We both wish to express our appreciation for the warm hospitality during visits to the University of Pittsburgh (B.S.) and to Saclay (F.T.). The research of F. T. was supported in part by the U.S. National Science Foundation.

APPENDIX A: SPIN OBSERVABLES RECALLED

The definition of the various spin observables are provided in the literature [4]. For convenience we present a brief discussion of the 16 observables.

The differential cross section is defined by

$$\sigma(\theta)=\frac{q}{k}\mathscr{I}(\theta),$$

with q the final and k the initial c.m. momenta. Here we extract the angle dependent function $\mathscr{I}(\theta)$, which is used in FTS to define ''profile functions.'' These profile functions are denoted by $\hat{X}=\mathscr{I}\times X$, for any spin observable X. The profile functions are determined by bilinear products of amplitudes and therefore are useful for extracting amplitude information.

Of the 16 observables, one is (1) the cross-section function $\mathscr{I}$; three are *single spin observables*; (2) the polarization

[9]We have not included the oft-quoted work of Ref. [12], since we found a serious error in their code; namely, their Q_ℓ functions are wrong. As a consequence, their spin observables display a large and incorrect number of nodes near threshold [13]. We appreciate receiving a copy of their code from C. Bennhold. This was a case where the general FTS threshold rules [4] served to detect an error and shows one way these rules can be useful.

of the produced Λ, $\hat{P}$; (3) the polarized target asymmetry, $\hat{T}$; and (4) the photon polarization asymmetry $\hat{\Sigma}$.

The remaining 12 spin observables are *double spin observables*. These are further classified as involving (BT) polarized beam, polarized target; (BR) polarized beam, polarized recoil Λ; (TR) polarized target, polarized recoil Λ. Each of these three types of double spin observables have four members. The (BR) type is also called a spin transfer observable. The (TR) type is also called a spin depolarization observable, often denoted by the symbol D; for example, the depolarization spin transfer variable where the incident p and the final Λ spin directions are normal (N) to the scattering plane is usually called D_{NN}. In the notation of FTS that spin variable is called $C^{p,\Lambda}_{y,y'}$. Their notation is based on the spin correlation description, where the superscript indicates the two particles involved (e.g., the BT, BR, or TR classification) and the subscript indicates direction. These directions are denoted by either the initial unit vectors, $\hat{x},\hat{y},\hat{z}$, or the final unit vectors, $\hat{x}',\hat{y}',\hat{z}'$. Another convention used is that of normal N, sideways S, and longitudinal L directions: $\hat{x}\equiv S,\hat{y}\equiv N,\hat{z}\equiv L$.

The relations between these spin-correlation (double spin) observables and the conventional set used here is for BT:

$$\hat{E}=C^{\gamma,p}_{z,z}, \quad \hat{H}=C^{\gamma,p}_{y,x},$$

$$\hat{F}=C^{\gamma,p}_{z,x}, \quad \hat{G}=C^{\gamma,p}_{y,z};$$

for BR:

$$\hat{C}_{z'}=C^{\gamma,\Lambda}_{z,z'}, \quad \hat{C}_{x'}=C^{\gamma,\Lambda}_{z,x'},$$

$$\hat{O}_{x'}=C^{\gamma,\ \Lambda}_{y,x'}\hat{O}_{z'}=C^{\gamma,\Lambda}_{y,z'};$$

and for TR:

$$\hat{L}_{z'}=C^{p,\Lambda}_{z,z'}, \quad \hat{L}_{x'}=C^{p,\Lambda}_{z,x'},$$

$$\hat{T}_{z'}=C^{p,\Lambda}_{x,z'}, \quad \hat{T}_{x'}=C^{p,\Lambda}_{x,x'}.$$

The Cartesian components refer to the spin axis for the baryons; for the photon they indicate either linear or circular polarization states (see Ref. [4] for a discussion).

APPENDIX B: PROJECTION OF MULTIPOLES

Argand plots of the electric $E^{\pm}_{\ell}$ and magnetic $M^{\pm}_{\ell}$ multipoles are obtained from the $CGLN$ amplitudes F_1,F_2,F_3, and F_4 by the following projection integrals:

$$E^{+}_{\ell}=\frac{1}{2(\ell+1)}\int_{-1}^{1}dx\Bigg(F_1P_{\ell}-F_2P_{\ell+1}+\frac{1}{\ell+1}(1-x^2)F_3P'_{\ell}+\frac{1}{\ell+2}(1-x^2)F_4P'_{\ell+1}\Bigg),$$

$$E^{-}_{\ell}=\frac{1}{2\ell}\int_{-1}^{1}dx\Bigg(-F_1P_{\ell}+F_2P_{\ell-1}+\frac{1}{\ell}(1-x^2)F_3P'_{\ell}+\frac{1}{\ell-1}(1-x^2)F_4P'_{\ell-1}\Bigg),$$

$$M^{+}_{\ell}=\frac{1}{2(\ell+1)}\int_{-1}^{1}dx\Bigg(F_1P_{\ell}-F_2P_{\ell+1}-\frac{1}{\ell(\ell+1)}(1-x^2)F_3P'_{\ell}\Bigg),$$

$$M^{-}_{\ell}=\frac{1}{2\ell}\int_{-1}^{1}dx\Bigg(-F_1P_{\ell}+F_2P_{\ell-1}+\frac{1}{\ell(\ell+1)}(1-x^2)F_3P'_{\ell}\Bigg). \tag{B1}$$

Here $x=\cos\theta$, P_{ℓ} are the Legendre polynomials, and the $CGLN$ amplitudes are given in Refs. [6,7], where they have been calculated using diagrammatic techniques in an isobaric approach.

[1] M. Bockhorst *et al.*, Z. Phys. C **63**, 37 (1994).

[2] See, e.g., R. A. Schumacher, Nucl. Phys. **A585**, 63c (1995).

[3] J. P. Bocquet *et al.*, in *Proceedings of the Particles and Nuclei XIII International Conference*, Perugia, 1993, edited by A. Pascolini (World Scientific, Singapore, 1994).

[4] C. G. Fasano, F. Tabakin, and B. Saghai, Phys. Rev. C **46**, 2430 (1992).

[5] F. Tabakin, Nucl. Phys. **A570**, 311c (1994); Cetin Savkli, M. Pichowsky, and F. Tabakin, Phys. Rev. C (to be published).

[6] R. A. Adelseck and B. Saghai, Phys. Rev. C **42**, 108 (1990).

[7] R. Williams, C. Ji, and S. Cotanch, Phys. Rev. C **46**, 1617 (1992).

[8] J.C. David, C. Fayard, G.H. Lamot, and B. Saghai, in *Proceedings of the 14th International Few-Body Conference*, Williamsburg, 1994, edited by F. Gross, AIP Conf. Proceedings No. 334 (AIP, New York, 1995).

[9] See, e.g., P. Collins, *An Introduction to Regge Theory and High Energy Physics* (Cambridge University Press, Cambridge, England, 1977).

[10] I. S. Barker, A. Donnachie, and J. K. Storrow, Nucl. Phys. **B25**, 179 (1970); **B95**, 347 (1975).

[11] J. Ajaka, P. Hoffmann-Rothe, B. Saghai, and F. Tabakin (unpublished).

[12] H. Tanabe, M. Kohno, and C. Bennhold, Phys. Rev. C **39**, 741 (1989).

[13] B. Saghai, in *Proceedings of the Sixth Workshop on Perspectives at Intermediate Energies*, Trieste, 1993, edited by S. Boffi, C. Ciofi degli Atti, and M. Giannini (World Scientific, 1994).

[14] R. Koniuk and N. Isgur, Phys. Rev. D **21**, 1868 (1980); S. Capstick and W. Roberts, **49**, 4570 (1994).